

## ARTICLE

<https://doi.org/10.1038/s42005-019-0180-2>

OPEN

# Signatures of structural differences in Pt-P- and Pd-P-based bulk glass-forming liquids

Oliver Gross<sup>1</sup>, Nico Neuber<sup>1</sup> , Alexander Kuball<sup>1</sup>, Benedikt Bochtler<sup>1</sup> , Simon Hechler<sup>1</sup>, Maximilian Frey<sup>1</sup> & Ralf Busch<sup>1</sup>

The structural differences between the compositionally related Pt-P- and Pd-P-based bulk glass-forming liquids are investigated in synchrotron X-ray scattering experiments. Although Pt and Pd are considered to be topologically equivalent in structural models, we show that drastic changes in the total structure factor and in the reduced pair distribution function are observed upon gradual substitution. These variations indicate the existence of significant structural differences on the short- (SRO) and medium-range order (MRO) length scale. The structural data suggest that the distribution of the dominant polyhedra and the distribution of their connection schemes gradually change from Pt-P- to Pd-P-based alloys, which is likely connected to the different sensitivities to annealing or cooling rate induced embrittlement. The evolution of the total structure factor and the reduced pair distribution function with increasing temperature indicate the (partial) dissolution of both, the MRO and the SRO, which reflects the thermodynamic properties of the liquids.

<sup>1</sup>Chair of Metallic Materials, Saarland University, Campus C6.3, 66123 Saarbrücken, Germany. Correspondence and requests for materials should be addressed to O.G. (email: [oliver.gross@uni-saarland.de](mailto:oliver.gross@uni-saarland.de))

Pt-P- and Pd-P-based bulk metallic glass (BMG) forming liquids feature a high glass-forming ability (GFA), which is reflected by their critical casting thicknesses ( $d_c$ ) usually exceeding  $1.5\text{ cm}^{1-3}$ . The compositional similarities (e.g.,  $\text{Pt}_{42.5}\text{Cu}_{27}\text{Ni}_{9.5}\text{P}_{21}$  and  $\text{Pd}_{43}\text{Cu}_{27}\text{Ni}_{10}\text{P}_{20}$ ), the interchangeability of Pt and Pd without losing the bulk GFA<sup>4,5</sup>, the topological equivalence of Pt and Pd<sup>6,7</sup>, and the similar kinetic fragility<sup>8-11</sup> suggest a close connection between Pt-P- and Pd-P-based liquids. However, the  $d_c$  of the alloy with the highest GFA in both systems varies by a factor of four from  $d_c = 20\text{ mm}$  for  $\text{Pt}_{42.5}\text{Cu}_{27}\text{Ni}_{9.5}\text{P}_{21}$  to  $d_c = 80\text{ mm}$  for the  $\text{Pd}_{42.5}\text{Cu}_{30}\text{Ni}_{7.5}\text{P}_{20}$  alloy<sup>1,2</sup>. This difference is attributed to the fact that the GFA of Pt-P-based BMG forming liquids originates from a high interfacial energy, compensating a high driving force for crystallization and a kinetically fragile behavior<sup>12,13</sup>. In contrast, the Pd-P-based liquids are rather stabilized by an extremely low-driving force for crystallization<sup>12</sup>, which can be approximated by the entropy of fusion  $\Delta S_f$ .  $\Delta S_f$  represents the negative slope of the Gibbs free energy difference between the liquid and the crystal at the liquidus temperature. Although not independent from the crystalline state, the large variation in  $\Delta S_f$  of about a factor of two ( $\Delta S_f(\text{Pt}_{42.5}\text{Cu}_{27}\text{Ni}_{9.5}\text{P}_{21}) = 12\text{ Jg}\cdot\text{atom}^{-1}\text{ K}^{-1}$ ,  $\Delta S_f(\text{Pd}_{43}\text{Cu}_{27}\text{Ni}_{10}\text{P}_{20}) = 5.8\text{ Jg}\cdot\text{atom}^{-1}\text{ K}^{-1}$ <sup>8,11,12</sup>) between Pt-P- and Pd-P-based alloys can probably not solely be traced back to different entropic states of the crystalline mixtures. It rather suggests that the two liquids possess different structural states in the equilibrium liquid. This hypothesis is supported by the observation of a rapidly ascending specific heat capacity in the liquid state ( $c_p$ ) upon undercooling the Pt-P-based liquids whereas that of the Pd-P-based alloy compositions ascends more slowly<sup>12</sup> (see also Supplementary Fig. 1). The excess heat capacity  $\Delta c_p^{l-x}(T)$ , representing the difference between the specific heat capacity of the liquid and the crystalline state, is connected to the rate of loss in the excess entropy  $\Delta S_{l-x}(T)$ . As  $\Delta S_{l-x}(T)$  is proportional to the configurational part of the entropy of the liquid<sup>14</sup>, the rate of change in  $\Delta S_{l-x}(T)$  indicates a more pronounced ordering process in Pt-P-based liquids upon undercooling. The connection between the ascending specific heat capacity and structural ordering has been shown in computer simulations<sup>15</sup>. These observations draw the picture of rather disordered Pt-P-based liquids at high temperatures, undergoing a rapid ordering upon approaching the glass transition. On the other hand, a large degree of local order is likely already present at high temperatures in the equilibrium liquid of the Pd-P-based compositions, reflected by the small entropy of fusion. Moreover, the existence of structural differences is suggested by the varying sensitivity to cooling rate induced and annealing induced embrittlement<sup>5,16</sup>. Kumar et al.<sup>5,16</sup> reported that the bending ductility of Pd-P-based glasses strongly depends on the cooling rate and the annealing protocol whereas the Pt-P-based glasses always showed plasticity. The partial replacement of Pd by Pt reduced the sensitivity of the alloys to cooling rate induced embrittlement<sup>5</sup>. These observations are attributed to different critical fictive temperatures ( $T_f^{\text{critical}}$ )<sup>16</sup>. The fictive temperature  $T_f$  is defined as the glass transition upon cooling and therefore depends on the applied cooling rate<sup>17</sup>.  $T_f$  of a glass can also be changed by annealing or rejuvenation<sup>18,19</sup>. However,  $T_f^{\text{critical}}$  is an inherent property of the alloy composition and should be connected to the structure of the glass. If a glass possesses a  $T_f$  below the  $T_f^{\text{critical}}$ , it will fracture without plastic deformation<sup>16</sup>.

In order to find implications of structural differences in the two systems that might explain the different thermodynamic and mechanical properties as well as the variation in the GFA, synchrotron X-ray scattering experiments in the glass, the supercooled liquid and the equilibrium liquid are conducted on  $\text{Pt}_{42.5}\text{Cu}_{27}\text{Ni}_{9.5}\text{P}_{21}$  and  $\text{Pd}_{43}\text{Cu}_{27}\text{Ni}_{10}\text{P}_{20}$ . Moreover, Pt is stepwise

replaced by Pd and the total structure factor as well as the reduced pair distribution function (PDF) are determined at ambient temperature, revealing the compositionally induced structural changes. The experiments on these multicomponent bulk glass-forming liquids can be considered as a top-down approach, complementing the computational modeling of less complex metallic liquids.

## Results

**The total structure factor at constant temperature.** Figure 1 shows the total structure factor  $S(Q)$  of the  $\text{Pt}_{42.5}\text{Cu}_{27}\text{Ni}_{9.5}\text{P}_{21}$  and the  $\text{Pd}_{43}\text{Cu}_{27}\text{Ni}_{10}\text{P}_{20}$  alloy composition at 323 K. The  $S(Q)$  of the  $\text{Pt}_{42.5}\text{Cu}_{27}\text{Ni}_{9.5}\text{P}_{21}$  glass exhibits a pronounced prepeak at  $\sim 2.1\text{ \AA}^{-1}$ , preceding the first sharp diffraction peak (FSDP), whereas the shoulder of the second diffraction peak towards higher  $Q$ -values is more pronounced for the  $\text{Pd}_{43}\text{Cu}_{27}\text{Ni}_{10}\text{P}_{20}$  alloy composition. In order to investigate the compositional effect on these two features, Pt in the  $\text{Pt}_{42.5}\text{Cu}_{27}\text{Ni}_{9.5}\text{P}_{21}$  alloy is gradually replaced by Pd, following the compositions displayed in Fig. 2. As shown in Fig. 2a, b, the intensity of the prepeak fades with decreasing Pt content and the shoulder at the second peak gains intensity. It should be noted that the samples used for the diffraction experiments at 298 K were cut from plates with the same dimension. Hence, they experienced similar cooling rates and the observed variations in  $S(Q)$  do not originate from differences in the thermal history.

**The total structure factor as a function of temperature.** The temperature-induced evolution of the total structure factor is shown for the  $\text{Pt}_{42.5}\text{Cu}_{27}\text{Ni}_{9.5}\text{P}_{21}$  and the  $\text{Pd}_{43}\text{Cu}_{27}\text{Ni}_{10}\text{P}_{20}$  composition in Fig. 3. Figure 3a, c display the low and Fig. 3b, d the high  $Q$ -region. The data at low temperatures were obtained upon heating a glassy sample (blue) and those at high temperature upon cooling the liquid from 1153 K (red). The temperature interval in-between the high and low temperature data is obscured by crystallization. The arrows indicate the evolution of the peak maxima and minima with decreasing temperature. For both alloy compositions it is observed that the peak intensities increase, and widths decrease which is on the one hand attributed to an increasing structural order and on the other hand to the decreasing atomic vibrations (Debye-Waller factor). The opposing movement of the first and second diffraction peak results in a virtually temperature invariant minimum in-between the two

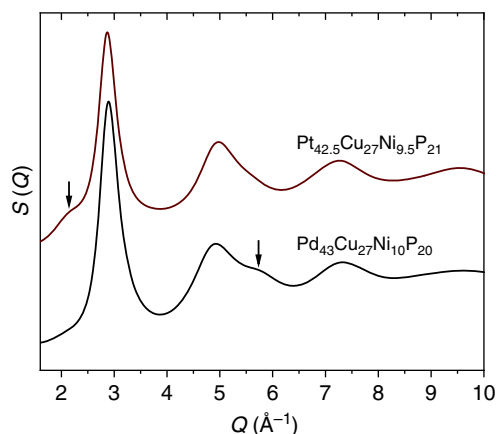


**Fig. 1** Total structure factor  $S(Q)$  of as-cast  $\text{Pt}_{42.5}\text{Cu}_{27}\text{Ni}_{9.5}\text{P}_{21}$  and  $\text{Pd}_{43}\text{Cu}_{27}\text{Ni}_{10}\text{P}_{20}$  at 323 K. At low  $Q$ -values ( $\sim 2.1\text{ \AA}^{-1}$ ) only  $\text{Pt}_{42.5}\text{Cu}_{27}\text{Ni}_{9.5}\text{P}_{21}$  exhibits a prepeak. The shoulder at the second peak ( $\sim 5.7\text{ \AA}^{-1}$ ) is distinctly more pronounced for the  $\text{Pd}_{43}\text{Cu}_{27}\text{Ni}_{10}\text{P}_{20}$  alloy composition

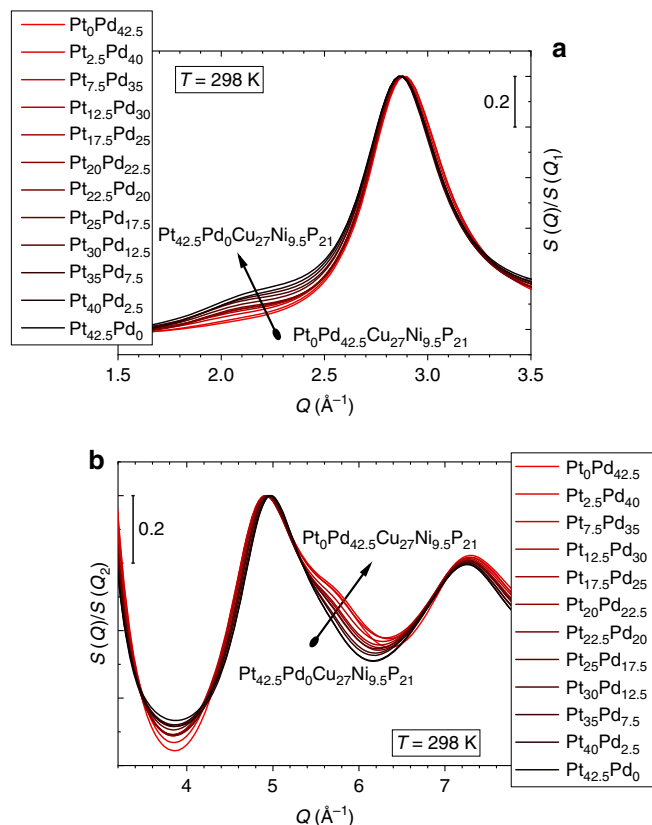


**Fig. 2** Total structure factor  $S(Q)$  of as-cast  $\text{Pt}_{42.5-x}\text{Pd}_x\text{Cu}_{27}\text{Ni}_{9.5}\text{P}_{21}$  samples, where  $x = 0, 2.5, 7.5, 12.5, 17.5, 20, 22.5, 25, 30, 35, 40$ , and  $42.5$ . **a, b** The dependence of the prepeak at  $\sim 2.1 \text{ \AA}^{-1}$  and the shoulder at  $\sim 5.7 \text{ \AA}^{-1}$  on the Pt-to-Pd ratio. With increasing Pd concentration, the prepeak in the low  $Q$ -range diminishes whereas the characteristic at  $5.7 \text{ \AA}^{-1}$  gets more pronounced. In **a, b**,  $S(Q)$  is normalized to the peak height of the first and second sharp diffraction peak  $S(Q_1)$  and  $S(Q_2)$ , respectively. The diffraction experiments were conducted at 298 K. All samples experienced similar cooling rates as they were cut from plates of the same dimension

peaks. The insets in Fig. 3a, c magnify the low  $Q$ -region of  $S(Q)$ . In the case of the  $\text{Pt}_{42.5}\text{Cu}_{27}\text{Ni}_{9.5}\text{P}_{21}$  liquid, the intensity of the prepeak decreases upon heating and vanishes in the equilibrium liquid (see also Supplementary Fig. 2). For the  $\text{Pd}_{43}\text{Cu}_{27}\text{Ni}_{10}\text{P}_{20}$  liquid, a comparable feature is not detected in the low  $Q$ -region. Instead, the shoulder at the second peak gets more pronounced as the temperature decreases.

**The reduced PDF.** In order to further investigate the structural differences in the two alloy families, the reduced PDF is calculated according to Eq. 4. Figure 4 shows the temperature-induced evolution of  $G(r)$  of  $\text{Pt}_{42.5}\text{Cu}_{27}\text{Ni}_{9.5}\text{P}_{21}$  and  $\text{Pd}_{43}\text{Cu}_{27}\text{Ni}_{10}\text{P}_{20}$  in the same temperature interval as indicated in Fig. 3. The arrows indicate the shifts of the peak maxima and minima with decreasing temperature. As commonly observed in metallic liquids, the first peak position, which is assumed to reflect the average, weighted nearest neighbor distance, shifts towards higher values with decreasing temperature. This intuitively physically unlikely behavior has been attributed to an increasing coordination number (CN) upon cooling<sup>20,21</sup>. However, Ding et al.<sup>22</sup> argued that the anomalous peak shift might originate from the asymmetry of the peak shape. If the skewness is considered, the mean bond length is found to increase with increasing temperature<sup>23</sup>.

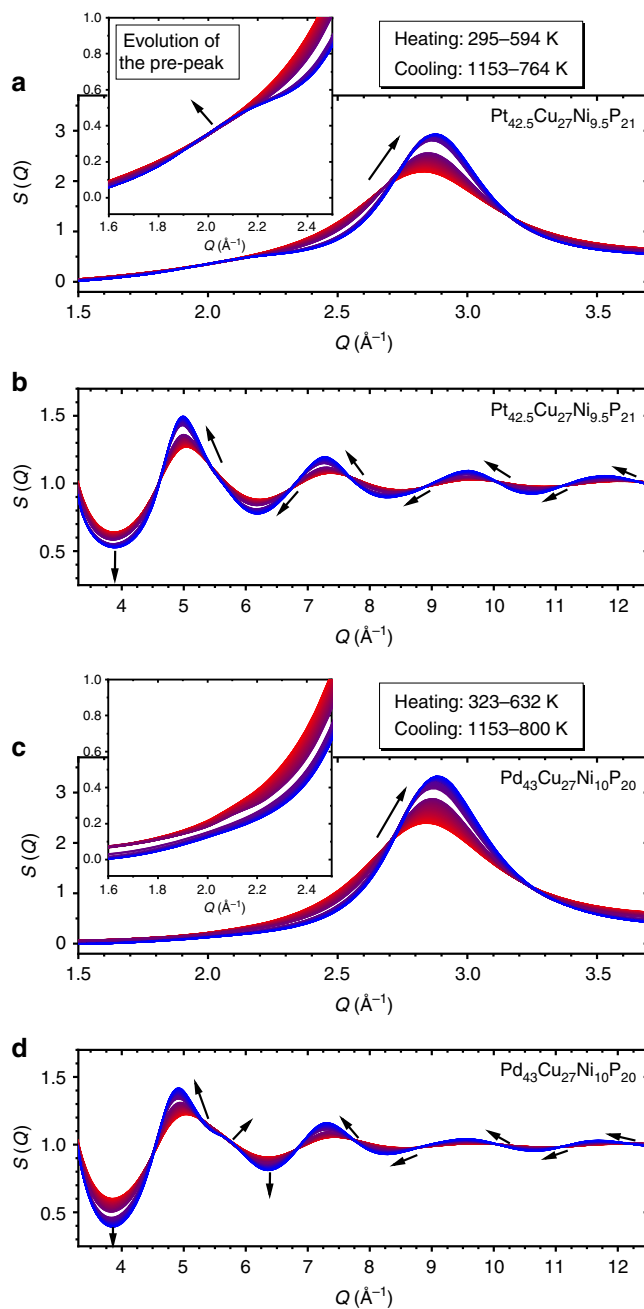


**Fig. 3** Temperature-induced change of the total structure factor  $S(Q)$ . **a, b, c, d** The total structure factor of  $\text{Pt}_{42.5}\text{Cu}_{27}\text{Ni}_{9.5}\text{P}_{21}$  and  $\text{Pd}_{43}\text{Cu}_{27}\text{Ni}_{10}\text{P}_{20}$  as a function of temperature. The high temperature data (red) were collected upon cooling from 1153 K and those at low temperatures (blue) upon heating from the glassy state. **a, c** show the low  $Q$ -range and the insets magnify the region where the prepeak in  $\text{Pt}_{42.5}\text{Cu}_{27}\text{Ni}_{9.5}\text{P}_{21}$  evolves with decreasing temperature. **b, d** show the oscillation of  $S(Q)$  at high  $Q$ -values. The second peak of  $S(Q)$  of both alloys is magnified in Supplementary Fig. 3. The arrows illustrate the evolution of the peak maxima and minima with decreasing temperature

The first peak position of  $\text{Pt}_{42.5}\text{Cu}_{27}\text{Ni}_{9.5}\text{P}_{21}$  and  $\text{Pd}_{43}\text{Cu}_{27}\text{Ni}_{10}\text{P}_{20}$  at 298 K is located at  $2.79$  and  $2.77 \text{ \AA}$ . As  $G(r)$  of the two alloy compositions is dominated by the Pt–Pt and the Pd–Pd partial PDFs (see Supplementary Figs. 4 and 5 and Supplementary Note 1), the first peak position represents in a first approximation the distance between two Pt and two Pd atoms, possessing an atomic radius of  $1.39$  and  $1.40 \text{ \AA}$ <sup>7</sup>. The most

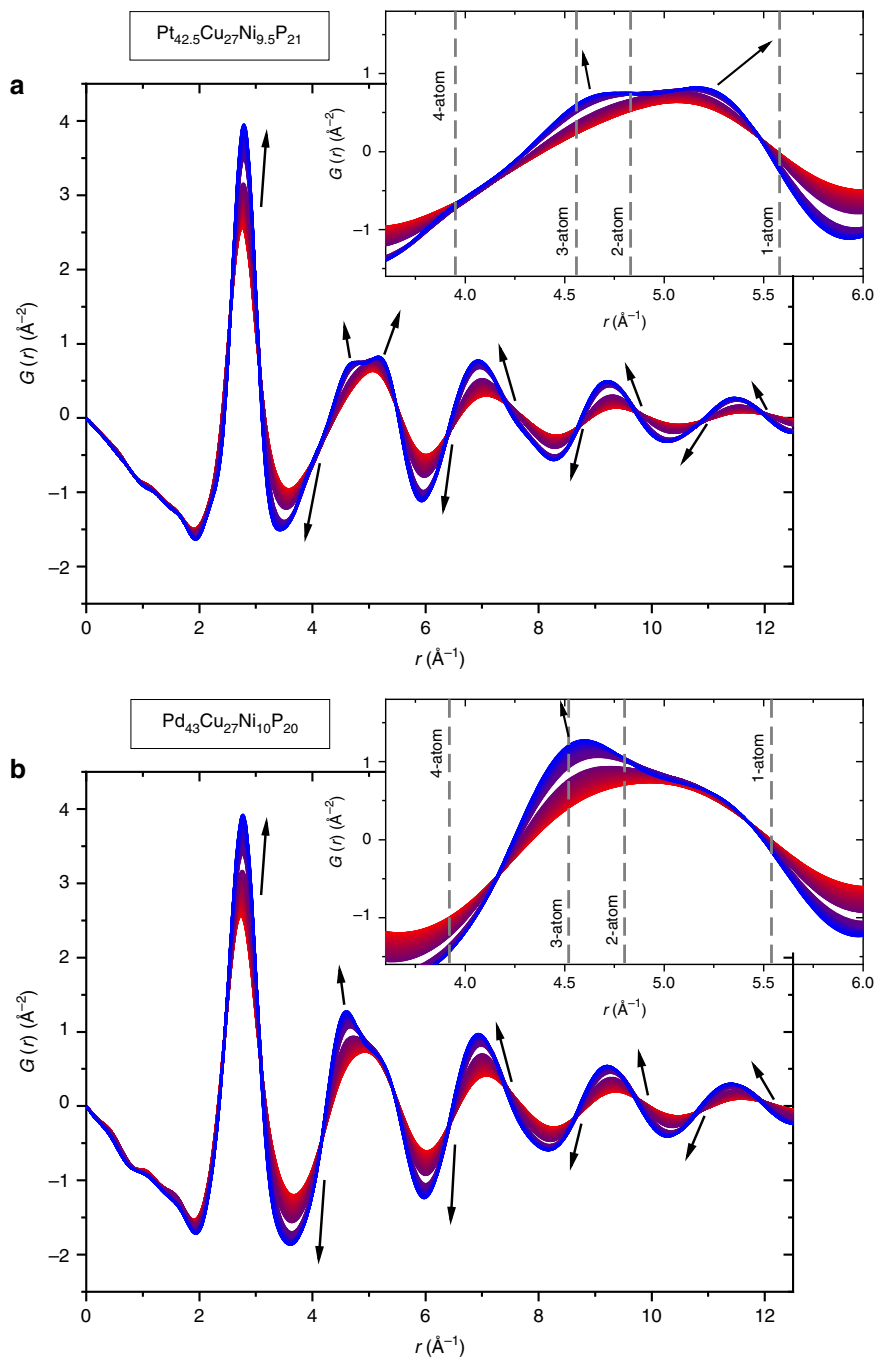


**Fig. 4** Reduced pair distribution function  $G(r)$  of **a**  $\text{Pt}_{42.5}\text{Cu}_{27}\text{Ni}_{9.5}\text{P}_{21}$  and **b**  $\text{Pd}_{43}\text{Cu}_{27}\text{Ni}_{10}\text{P}_{20}$  as a function of temperature. The high temperature data (red) were collected upon cooling from 1153 K and those at low temperatures (blue) upon heating from the glassy state. The arrows indicate the evolution of the peak maxima and minima with decreasing temperature. The insets magnify the second peak, corresponding to the second nearest neighbor distances. The vertical lines in the inset mark the most probable second nearest neighbor distances if adjacent clusters share one, two, three, or four atoms, calculated from the first peak position

distinct difference in  $G(r)$  of the two alloys is observed at the second peak, reflecting the distances in the second nearest neighbor shell. In both cases, the second peak changes its shape and sharpens with decreasing temperature. The insets in Fig. 4, magnifying the temperature-induced evolution of the second peak, show that two peak maxima evolve for the  $\text{Pt}_{42.5}\text{Cu}_{27}\text{Ni}_{9.5}\text{P}_{21}$  liquid, whereas a single maximum with a pronounced shoulder on the high- $r$  side forms for the  $\text{Pd}_{43}\text{Cu}_{27}\text{Ni}_{10}\text{P}_{20}$  alloy composition. The compositional variation of  $G(r)$  on the Pt–Pd axis at ambient temperature is shown in Fig. 5. Again, the changes

at the second peak of  $G(r)$  upon substitution of Pd by Pt are obvious and are magnified in the inset of Fig. 5. The vertical lines in the insets of Figs. 4a, b and 5 are referred to in the discussion section.

### Discussion

Although Pt and Pd atoms are considered to be topologically equivalent in structural models<sup>6,7</sup>, the variations observed in  $S(Q)$  and  $G(r)$  suggest major structural differences. As the FSDP in

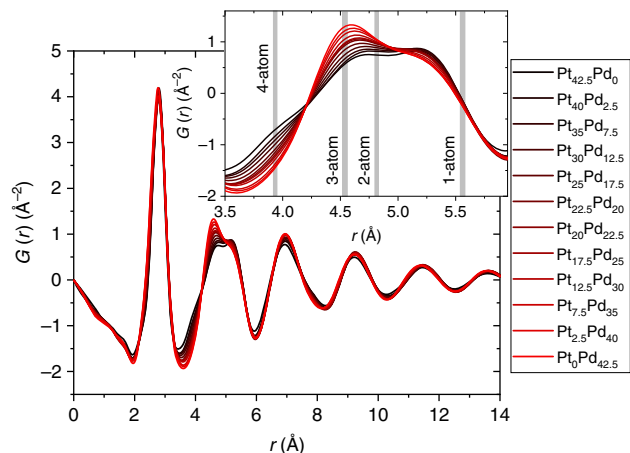


**Fig. 5** Compositional variation of the reduced pair distribution function  $G(r)$  of Pt/Pd-P-based glasses at 298 K. The inset magnifies the second peak corresponding to the second nearest neighbor distances. The gray areas in the inset mark the most probable second nearest neighbor distances if adjacent clusters share one, two, three, or four atoms calculated from the first peak positions

$S(Q)$  already contains information on the medium-range order (MRO) of the liquid<sup>24</sup>, the presence of a prepeak indicates a distinctly pronounced MRO<sup>25</sup> and is observed in various liquids<sup>26–32</sup>. Cheng et al.<sup>25</sup> concluded from experimental observations that the detection of a prepeak in  $S(Q)$  is likely if the concentration of solutes is low (solute-lean composition) and if the solute specie possesses a high atomic form factor (“strong scatterer”). The type of MRO that results from these two statements is based on the avoidance of solute–solute bindings. Solute atoms, being the center of the representative cluster, form a sublattice-like structure that becomes visible as a prepeak in  $S(Q)$  if the weighting factor of the solute–solute partial structure factor is sufficiently large<sup>25</sup>. Such a prepeak is detected in binary Zr–Pt liquids (solute-lean, e.g.,  $Zr_{80}Pt_{20}$ )<sup>27,33</sup>. It originates from the spatial arrangement of the Pt-centered clusters and hence from the noble metal–noble metal correlations<sup>27,33</sup>. As reported by Mauro et al.<sup>34</sup>, the prepeak at low  $Q$ -values vanishes if Pt is replaced by Pd. It was noticed that this observation is not equatable to the dissolution of the MRO as the lower atomic form factor of Pd in comparison to Pt might solely reduce the detectability of the prepeak (see Eqs. 2 and 3 in “Methods”) <sup>34</sup>.

Based on the discussion above, the type of MRO prevailing in  $Pt_{42.5}Cu_{27}Ni_{9.5}P_{21}$  might be different as the composition can be considered as solute rich<sup>35</sup>. The existence of a prepeak for a solute-rich glass has previously been reported in the  $Ce_{55}Al_{45}$  alloy composition<sup>36</sup>. Despite from the type of MRO prevailing in  $Pt_{42.5}Cu_{27}Ni_{9.5}P_{21}$ , the question arises if the disappearance of the prepeak in  $Pd_{43}Cu_{27}Ni_{10}P_{20}$  only results from the variation of the atomic form factors of Pd and Pt. In the following section, possible origins of the prepeak are discussed, suggesting that the varying atomic form factor should not result in the disappearance of the prepeak.

The  $S(Q)$  of the  $Pt_{42.5}Cu_{27}Ni_{9.5}P_{21}$  is dominated by the Pt–Pt and Pt–Cu partial structure factors (Supplementary Fig. 4) and the prepeak most probably originates from one of the two partials. In a previous study, the authors observed that other Pt–P-based alloy compositions with a larger Pt and lower Cu content (i.e.,  $Pt_{60}Cu_{16}Co_2P_{22}$  and  $Pt_{57.3}Cu_{14.6}Ni_{5.3}P_{22.8}$ ) do not feature a prepeak at low  $Q$ -values<sup>8</sup>. If the prepeak arises from the Pt–Cu partial, an increasing Pt and a decreasing Cu content would increase the significance of the Pt–Pt partial structure factor,

making the Pt–Cu correlations less dominant. Another possibility is that the MRO results from the Pt–Pt correlations as the Pt atoms in  $Pt_{42.5}Cu_{27}Ni_{9.5}P_{21}$  are on average more often separated by a distance larger than the first coordination shell due to the larger amount of Cu, Ni, and P atoms. In the case of higher Pt-concentrations, the Pt atoms are less diluted, and they are more frequently nearest neighbors to each other, reducing the significance of the MRO. As the dominant partial structure factors in  $Pd_{43}Cu_{27}Ni_{10}P_{20}$  and  $Pd_{42.5}Cu_{27}Ni_{9.5}P_{21}$  are Pd–Pd and Pd–Cu, equivalent to Pt–Pt and Pt–Cu in  $Pt_{42.5}Cu_{27}Ni_{9.5}P_{21}$  (Supplementary Figs. 4 and 5), the disappearance of the prepeak (Figs. 1 and 2) and the evolving shoulder at the second peak are most likely not traced back to the changing form factor as suggested for the Zr–Pd liquids. The varying signatures in  $S(Q)$  rather suggest that the distribution of the local representative structural units (cluster types) and their spatial arrangements in Pt–P- and Pd–P-based liquids vary as discussed in more detail in the following.

The existence of a shoulder at the second peak of  $S(Q)$  has been attributed to icosahedral short-range order (SRO). In the case of perfect icosahedral SRO, the ratio between the first two peak positions  $Q_2/Q_1$  and the ratio between the first peak position and the location of the shoulder  $Q_{\text{shoulder}}/Q_1$  is 1.71 and 2.04<sup>37,38</sup>. The location of the shoulder of the second peak of  $S(Q)$  of  $Pd_{43}Cu_{27}Ni_{10}P_{20}$  is determined by fitting, using a two Gaussian function.  $Q_2/Q_1$  and  $Q_1/Q_{\text{shoulder}}$  for the  $Pd_{43}Cu_{27}Ni_{10}P_{20}$  composition are 1.71 and 1.96, which is in good agreement with the expected values, indicating a little distortion of the icosahedral SRO<sup>37</sup>. In the  $Pd_{40}Ni_{40}P_{20}$  BMG forming liquid, tricapped trigonal prisms coexisting with Ni-centered icosahedra are found as representative structural units, supporting the idea of an at least partially icosahedral SRO in  $Pd_{43}Cu_{27}Ni_{10}P_{20}$  and  $Pd_{42.5}Cu_{27}Ni_{9.5}P_{21}$ <sup>39</sup>. Moreover, Park et al.<sup>40</sup> determined a CN of 11.4 in  $Pd_{40}Ni_{40}P_{20}$  and 12.6 in  $Pd_{40}Cu_{30}Ni_{10}P_{20}$  around the Ni atoms, which are close to values of a perfect icosahedron ( $CN = 12$ ). From a topological point of view, the ratios between the atomic radii of Pt (139 pm<sup>7</sup>), Pd (140 pm<sup>7</sup>), and Cu/(Ni) (126 pm<sup>7</sup>) suggest icosahedral SRO around the Cu/(Ni) atoms in both liquids<sup>41</sup>. The more pronounced shoulder at the second peak of  $S(Q)$  in the  $Pd_{43}Cu_{27}Ni_{10}P_{20}$  and the  $Pd_{42.5}Cu_{27}Ni_{9.5}P_{21}$  liquid might therefore indicate a larger fraction of icosahedral SRO. In the case of the  $Pt_{42.5}Cu_{27}Ni_{9.5}P_{21}$  alloy composition, the existence of a comparable shoulder in  $S(Q)$  can only be guessed (see Fig. 1). Following the simulations of Guan et al.<sup>39</sup> on the compositional induced structural changes in the Pd–Ni–P system, the substitution of Pd by Pt might change the ratio between the two structural units, the trigonal prism, and the icosahedron.

As Fig. 3 reveals, a change in temperature influences both the MRO as well as the SRO. At temperatures above the liquidus temperature ( $T_l(Pt_{42.5}Cu_{27}Ni_{9.5}P_{21}) = 874\text{ K}$ <sup>8</sup>,  $T_l(Pd_{43}Cu_{27}Ni_{10}P_{20}) = 866\text{ K}$ <sup>12</sup>), the prepeak in  $Pt_{42.5}Cu_{27}Ni_{9.5}P_{21}$  vanishes and the shoulder at the second peak in  $S(Q)$  of  $Pd_{43}Cu_{27}Ni_{10}P_{20}$  becomes less prominent (Fig. 3). The disappearance of the prepeak in  $Pt_{42.5}Cu_{27}Ni_{9.5}P_{21}$  in the equilibrium liquid state, together with the large  $\Delta S_f$  and the rapidly ascending  $c_p^l$  upon cooling (Supplementary Fig. 1), suggest a significant reduction or the entire dissolution of the MRO. In the case of the (at least partially) icosahedral SRO in  $Pd_{43}Cu_{27}Ni_{10}P_{20}$  it is well known that this type of SRO prevails in many metallic glass-forming liquids (even above  $T_l$ ) and gets more pronounced as the glass transition is approached upon cooling<sup>42–45</sup>. Once more it should be emphasized that the reduced significance of both characteristics upon heating is on the one hand traced back to the dissolution of atomic order and on the other hand affected by the increasing atomic vibrations, diminishing the peak intensity<sup>46</sup>. However, in the case of the prepeak it has been observed in other metallic liquids that it remains visible even hundreds of Kelvin above

$T_f^{29,33}$ , supporting the idea of the dissolution of atomic order in  $Pt_{42.5}Cu_{27}Ni_{9.5}P_{21}$  in the equilibrium liquid.

The splitting of the second peak of the pair PDF (Figs. 4a, b and 5) reflecting the variety in the second nearest neighbor distances, has been observed in different metallic liquids<sup>47–49</sup>. In computer simulations it is suggested that the peak splitting originates from the uneven distribution of different types of cluster connections<sup>49,50</sup>. The local representative structural units may share one, two, three, and four atoms<sup>49,50</sup> and the most probable position of the second nearest neighbor for each cluster connection scheme according to these simulations can be calculated from the average bond length as  $2 r_1$  (1-atom connection),  $\sqrt{3} r_1$  (2-atom connection),  $\sqrt{8/3} r_1$  (3-atom connection), and  $\sqrt{2} r_1$  (4-atom connection)<sup>49,51</sup>. As value for  $r_1$ , the first peak position of the reduced PDF is chosen, mainly representing the noble metal–noble metal correlations. The obtained positions for the second nearest neighbor are depicted as vertical dashed lines in the inset in Fig. 4a, b. For topological reasons the more atoms the clusters share the smaller is the second nearest neighbor distance. The effect of the Pt/Pd concentration on the shape of the second peak at ambient temperature is magnified in the inset in Fig. 5. The calculated second nearest neighbor positions indicate that the distribution of connection schemes gradually changes as Pt is replaced by Pd. In the Pd–P-based glass, the peak at  $\sim 4.5$  Å seems to result from central atoms whose clusters are connected via face sharing (3-atom connection). As can be seen in Fig. 5, face sharing becomes less dominant upon substituting Pd by Pt. Instead the 1-atom and 2-atom connection schemes gain importance. The evolving shoulder at  $\sim 3.9$  Å suggests that even the 4-atom connection scheme is facilitated by the replacement of Pd. Although these cluster connection schemes are thought to already exist in the high temperature liquid and the peak splitting is smeared out by the thermal vibrations, the structural ordering occurring during cooling also affects the distribution of the cluster connection schemes<sup>49</sup>. Therefore, the sharpening of the features of the second peak observed in Fig. 4 is again attributed to the decreasing atomic vibrations and to the growing portion of certain cluster connection schemes at the expense of others, increasing the packing density of the liquid<sup>49,50</sup>. In the case of  $Pd_{43}Cu_{27}Ni_{10}P_{20}$ , the 3-atom cluster connections seem to prevail, and its fraction increases upon cooling whereas the structural data of  $Pt_{42.5}Cu_{27}Ni_{9.5}P_{21}$  suggest a larger diversity of cluster connection schemes. Against the background of an at least partially icosahedral SRO in  $Pd_{43}Cu_{27}Ni_{10}P_{20}$  (suggested by the shoulder at the second peak of  $S(Q)$ ), the existence of a variety of the 3-atom connections is reasonable as each (perfect) icosahedral cluster features 20 triangular faces, which adjacent clusters may share. In contrast, the representative structural units in  $Pt_{42.5}Cu_{27}Ni_{9.5}P_{21}$  might comprise a large fraction of trigonal prisms that connect via edge sharing (2-atom connection) as suggest by Gaskell for metal–metaloid glasses<sup>52</sup>. A distinct diversity of cluster connection schemes in the  $Pt_{42.5}Cu_{27}Ni_{9.5}P_{21}$  liquid including a larger portion of the more flexible 1-, 2-, and 4-atom connections would result in a higher configurational entropy of the liquid, contributing to, and agreeing with the experimentally measured, high  $\Delta S_f$  of the Pt–P-based liquids.

Following the argumentation of Guan et al.<sup>39</sup>, the coexistence of two structural units, the trigonal prism and the icosahedron, might be responsible for the good GFA in both systems. However, our structural investigations indicate that the ratio between both structural motifs changes upon substituting Pd by Pt. In the case of the Pd–P-based liquids, the icosahedral SRO is more dominant, leading to an increase of the 3-atom connections. In contrast, the prevalence of the trigonal prisms in the Pt–P-based liquids results in a broader distribution of the connection schemes.

Although the experimental findings discussed above are in striking accordance with the simulations performed by Ding et al.<sup>49</sup>, it should be noted that the shape of the second peak in  $G(r)$  of complex, multicomponent metallic liquids is also affected by the number of small atoms in the first coordination shell that may be involved in the cluster connection. As the partial reduced PDFs are not accessible in the conducted experiments, the contribution of the atoms possessing a much smaller atomic form factor than the noble metals has to remain unclear. Therefore, this study should be considered as top-down approach building a bridge between the experimental and computational material science on metallic glasses and relating the structural features of these bulk glass-forming metallic liquids to their thermodynamic and mechanical properties.

At this point one might speculate that the different distribution of the cluster connection schemes is related to the different sensitivity to annealing or cooling rate induced embrittlement of the two alloy families. When the sensitivity to embrittlement becomes more pronounced as Pt is partially replaced by Pd<sup>5</sup>, it might be a consequence of the increase of 3-atom connections in the Pd–P-based glasses. Interestingly, Ding et al.<sup>49</sup> reported in their simulations that the various cluster connection schemes react differently on external stresses. Clusters that are connected via 2- and 4-atom are more flexible as their local deformation exceeds that of the macroscopic strain, whereas clusters sharing 1-atom experience an almost identical strain. In contrast, the local strain of clusters with 3-atom connections is the smallest and remains below the microscopically imposed shear strain<sup>49</sup>. In other words, the simulations suggest that 3-atom connections are stiffer than the other connection schemes. Hence, the fraction of 3-atom connections, which increases upon increasing the Pd concentration or which should increase upon annealing and upon reducing the cooling rate, might exceed a critical value if the fictive temperature of the glass (defined as the glass transition upon cooling) falls below the critical fictive temperature  $T_f^{crit}$  (fictive temperature of the glass below which the sample embrittles)<sup>16</sup>.  $T_f^{crit}$  is also connected to an alloy specific critical value in the configurational entropy. Although the macroscopic  $G/B$  ratio ( $G$  = shear modulus,  $B$  = bulk modulus) for both alloy classes remains below the critical value of 0.41<sup>5,53</sup> at which the transition from a ductile to brittle behavior is suggested<sup>54</sup>, the locally increasing stiffness through the ascending portion of 3-atom connections in  $Pd_{43}Cu_{27}Ni_{10}P_{20}$  and  $Pd_{42.5}Cu_{27}Ni_{9.5}P_{21}$  might hamper the formation of multiple shear bands and increase the sensitivity to crack initiation and propagation.

In summary, the conducted synchrotron X-ray scattering experiments on the Pt–P- and Pd–P-based liquids suggest the existence of major structural differences in the two compositionally related alloy families. The comparison of the total structure factor of  $Pt_{42.5}Cu_{27}Ni_{9.5}P_{21}$  and  $Pd_{43}Cu_{27}Ni_{10}P_{20}$  indicate that significant structural differences exist. The total structure factor of the  $Pt_{42.5}Cu_{27}Ni_{9.5}P_{21}$  glass exhibits a distinct prepeak preceding the FSDP, implying the existence of a pronounced MRO. In contrast, the  $Pd_{43}Cu_{27}Ni_{10}P_{20}$  glass does not show a comparable feature, however, a shoulder at the second peak is observed, indicating at least partially icosahedral SRO. Both structural signatures suggest that the distribution of the representative structural units and their spatial arrangement in both families vary. In Pd–P-based liquids icosahedral SRO dominates, whereas the Pt–P-based liquids contain a larger fraction of trigonal prisms. Upon gradually replacing Pt by Pd, the prepeak fades and the shoulder at the second peak gains intensity, suggesting that the ratio between icosahedra and trigonal prisms is changing. When approaching the equilibrium liquid state upon heating, the prepeak vanishes, and the shoulder gets less pronounced which is on the one hand attributed the

increasing atomic vibrations and on the other hand to the dissolution of atomic SRO and MRO. The disappearance of the prepeak in combination with the rapidly descending specific heat capacity of the liquid with increasing temperature and the large entropy of fusion draws the picture of a rather disordered  $\text{Pt}_{42.5}\text{Cu}_{27}\text{Ni}_{9.5}\text{P}_{21}$  liquid at high temperatures. This disordered liquid experiences a rapid ordering process involving the formation of MRO upon approaching the glass transition. The low entropy of fusion and the shallowly ascending specific heat capacity of the liquid upon cooling suggest that the structure of the  $\text{Pd}_{43}\text{Cu}_{27}\text{Ni}_{10}\text{P}_{20}$  liquid in the stable equilibrium already comprises a certain degree of SRO. The appearance of the second peak in the reduced PDF suggests that Pt–P- and Pd–P-based liquids possess different distributions of cluster connection schemes, resulting from the varying ratio between the two representative structural units. Pt–P-based liquids feature a broad distribution of cluster connection schemes, comprising the more flexible 2- and 4-atom connections, whereas the stiffer 3-atom connections prevail in the Pd–P-based liquids, originating from the more dominant icosahedral SRO. The varying distribution of connection schemes contribute to the large difference in the entropy of fusion and are likely to be associated to the different sensitivity to annealing or cooling rate induced embrittlement, with the Pd–P-based alloys being more prone to embrittlement.

## Methods

**Sample preparation.** In a first step, a prealloy is produced from the high-purity elements (purity > 99.95 wt%), Pt/Pd, Cu, and Ni. The elements are alloyed in an arc-furnace under a Ti-gettered high-purity Ar atmosphere. The prealloy is molten several times to ensure a homogeneous distribution of the elements. Subsequently, the prealloy is placed on top of the red P pieces in a fused silica tube of 1-m length, with an inner diameter of 12 mm and a wall thickness of 1.5 mm and heated inductively under high-purity Ar. A fluxing process is conducted by heating the alloys with dehydrated  $\text{B}_2\text{O}_3$  up to 1473 K in a 1-m-long fused silica tube with an inner diameter of 16 mm and a wall thickness of 1.5 mm. The alloys are held at this temperature for at least 6 h. If the overall mass loss during the complete alloying process is attributed to the loss of P, a maximum deviation of 0.5 at% P is estimated. In general, the preparation process is similar to the one of S-containing BMGs, described in detail in references<sup>55,56</sup>. Amorphous samples are produced from the purified alloys by casting them in water cooled copper molds using a custom build suction casting device. The alloy compositions containing Pt and Pd are obtained by mixing appropriate masses of the  $\text{Pt}_{42.5}\text{Cu}_{27}\text{Ni}_{9.5}\text{P}_{21}$  and  $\text{Pd}_{42.5}\text{Cu}_{27}\text{Ni}_{9.5}\text{P}_{21}$  alloy compositions. The  $\text{Pt}_{42.5}\text{Cu}_{27}\text{Ni}_{9.5}\text{P}_{21}$  and the  $\text{Pd}_{43}\text{Cu}_{27}\text{Ni}_{10}\text{P}_{20}$  samples that are heated to the equilibrium liquid and cooled at 0.333 K/s are cast as rods with a diameter of ~1.1 mm. In order to fit into  $\text{SiO}_2$  capillaries for the synchrotron X-ray experiments, the diameter of the rods is reduced by grinding. The samples for measurements at ambient temperature are cut from amorphous plate-shaped samples with a dimension of  $1 \times 10 \times 13 \text{ mm}^3$ .

**Synchrotron X-ray scattering experiments.** The X-ray scattering experiments are carried out at the high resolution beamline P02.1 at PETRA III at the Deutsches Elektronen Synchrotron (DESY) in Hamburg<sup>57</sup>. A wavelength of 0.207 Å (60 keV) and a beam size of  $0.5 \times 0.5 \text{ mm}^2$  is used. The samples are positioned in  $\text{SiO}_2$  capillaries with a diameter of 1 mm and a wall thickness of 0.01 mm and placed in a ceramic heater and heated at a rate of 0.333 K/s under a constant flow of high-purity Ar. The temperature calibration of the furnace is performed using Si powder. The measurements are carried out in transmission mode using a Perkin Elmer XRD1621 CsI bonded amorphous silicon detector (2048 pixels  $\times$  2048 pixels). The dark-subtracted, two-dimensional X-ray diffraction patterns are integrated using the Fit2D data analysis software<sup>58</sup>. The data are further processed using the PDFgetX2 software<sup>59</sup>. The background is measured at room temperature, assumed to be constant upon heating and cooling and subtracted from the integrated intensity data. The data are corrected for sample absorption, polarization, and multiple scattering. The total structure factor  $S(Q)$  is calculated as<sup>46</sup>

$$S(Q) = 1 + \frac{I_c(Q) - f(Q)^2}{f(Q)^2}, \quad (1)$$

where  $I_c(Q)$  is the coherently scattered intensity and  $f(Q)$  is the atomic form factor, and  $Q$  is the scattering vector. The angle brackets denote a compositional average over all constituents.  $S(Q)$  contains all the structural information and is composed of  $n(n+1)/2$  partial structure factors<sup>60</sup>,

$$S(Q) = \sum_{i \leq j} w_{ij} S_{ij}(Q) \quad (2)$$

where  $w_{ij}$  is the weighting factor expressed as

$$w_{ij} = \frac{c_i c_j f_i(Q) f_j(Q)}{f(Q)^2} \quad (3)$$

where  $c_i$  and  $c_j$  are the molar concentration of element  $i$  and  $j$ . The Fourier transform of the total structure factor yields the reduced PDF,

$$G(r) = \frac{2}{\pi} \int_0^\infty Q[S(Q) - 1] \sin(Qr) dQ \quad (4)$$

where  $r$  is the distance to the reference atom. Each  $G(r)$  pattern was optimized using an optimization algorithm in PDFgetX2 as described by Wei et al.<sup>61</sup>. As shown in Supplementary Fig. 6, the splitting of the second peak in  $G(r)$ , which is discussed in the main text, only becomes apparent if the maximum  $Q$ -range ( $Q_{\text{max}}$ ) for the Fourier transformation of  $S(Q)$  is beyond  $12 \text{ \AA}^{-1}$ . In contrast, the third and fourth peak in  $G(r)$  remain rather unaffected if  $Q_{\text{max}}$  is varied within 10.5 and  $16 \text{ \AA}^{-1}$  as already observed by Ma et al.<sup>24</sup> for even lower  $Q_{\text{max}}$ -values.

## Data availability

Raw data were generated at DESY (Hamburg, Germany) at the PETRA III (P02.1 beamline). Derived data supporting the findings of this study are available from the corresponding author on reasonable request.

Received: 9 January 2019 Accepted: 11 June 2019

Published online: 19 July 2019

## References

- Schroers, J. & Johnson, W. L. Highly processable bulk metallic glass-forming alloys in the Pt–Co–Ni–Cu–P system. *Appl. Phys. Lett.* **84**, 3666 (2004).
- Nishiyama, N. et al. The world's biggest glassy alloy ever made. *Intermetallics* **30**, 19–24 (2012).
- Na, J. H. et al. Bulk platinum-copper-phosphorus glasses bearing boron, silver, and gold. US10036087B2 (2018).
- Takeuchi, A. et al.  $\text{Pd}_{30}\text{Pt}_{20}\text{Cu}_{20}\text{Ni}_{20}\text{P}_{20}$  high-entropy alloy as a bulk metallic glass in the centimeter. *Intermetallics* **19**, 1546–1554 (2011).
- Kumar, G., Prades-Rodel, S., Blatter, A. & Schroers, J. Unusual brittle behavior of Pd-based bulk metallic glass. *Scr. Mater.* **65**, 585–587 (2011).
- Miracle, D. B. A structural model for metallic glasses. *Nat. Mater.* **3**, 697–702 (2004).
- Laws, K. J., Miracle, D. B. & Ferry, M. A predictive structural model for bulk metallic glasses. *Nat. Commun.* **6**, 8123 (2015).
- Gross, O. et al. The kinetic fragility of Pt–P- and Ni–P-based bulk glass-forming liquids and its thermodynamic and structural signature. *Acta Mater.* **132**, 118–127 (2017).
- Gallino, I., Gross, O., Dalla Fontana, G., Evenson, Z. & Busch, R. On the kinetic and thermodynamic fragility of the  $\text{Pt}_{60}\text{Cu}_{16}\text{Co}_2\text{P}_{22}$  and  $\text{Pt}_{57.3}\text{Cu}_{14.6}\text{Ni}_{5.3}\text{P}_{22.8}$  bulk metallic glasses. *J. Alloy. Compd.* **615**, S35–S39 (2014).
- Kato, H. et al. Fragility and thermal stability of Pt- and Pd-based bulk glass forming liquids and their correlation with deformability. *Scr. Mater.* **54**, 2023–2027 (2006).
- Gallino, I., Schroers, J. & Busch, R. Kinetic and thermodynamic studies of the fragility of bulk metallic glass forming liquids. *J. Appl. Phys.* **108**, 063501 (2010).
- Gross, O. et al. On the high glass-forming ability of Pt–Cu–Ni/Co–P-based liquids. *Acta Mater.* **141**, 109–119 (2017).
- Legg, B. A., Schroers, J. & Busch, R. Thermodynamics, kinetics, and crystallization of  $\text{Pt}_{57.3}\text{Cu}_{14.6}\text{Ni}_{5.3}\text{P}_{22.8}$  bulk metallic glass. *Acta Mater.* **55**, 1109–1116 (2007).
- Martinez, L.-M. & Angell, C. A. A thermodynamic connection to fragility of glass-forming liquids. *Nature* **410**, 663–667 (2001).
- Ding, J., Cheng, Y. Q., Sheng, H. & Ma, E. Short-range structural signature of excess specific heat and fragility of metallic-glass-forming supercooled liquids. *Phys. Rev. B* **85**, 1–5 (2012).
- Kumar, G., Neibecker, P., Liu, Y. H. & Schroers, J. Critical fictive temperature for plasticity in metallic glasses. *Nat. Commun.* **4**, 1536 (2013).
- Angell, C. A. Glass transition. *Encycl. Mater. Sci. Technol.* **4**, 3565–3575 (2001).
- Pan, J. et al. Extreme rejuvenation and softening in a bulk metallic glass. *Nat. Commun.* **9**, 560 (2018).
- Ketkaew, J. et al. Mechanical glass transition revealed by the fracture toughness of metallic glasses. *Nat. Commun.* **9**, 3271 (2018).
- Lou, H. et al. Negative expansions of interatomic distances in metallic melts. *Proc. Natl Acad. Sci. USA* **110**, 10068–10072 (2013).

21. Gangopadhyay, A. K. et al. Anomalous thermal contraction of the first coordination shell in metallic alloy liquids. *J. Chem. Phys.* **140**, 044505 (2014).
22. Ding, J. et al. Temperature effects on atomic pair distribution functions of melts. *J. Chem. Phys.* **140**, 064501 (2014).
23. Sukhomlinov, S. V. & Müser, M. H. Determination of accurate, mean bond lengths from radial distribution functions. *J. Chem. Phys.* **146**, 024506 (2017).
24. Ma, D., Stoica, A. D. & Wang, X.-L. Power-law scaling and fractal nature of medium-range order in metallic glasses. *Nat. Mater.* **8**, 30–34 (2009).
25. Cheng, Y. Q. & Ma, E. Atomic-level structure and structure-property relationship in metallic glasses. *Prog. Mater. Sci.* **56**, 379–473 (2011).
26. Nakamura, T. et al. Structural study in amorphous Zr-noble metal (Pd, Pt and Au) alloys. *J. Non-Cryst. Solids* **312–314**, 517–521 (2002).
27. Sordelet, D. J. et al. Structure of Zr x Pt100-x metallic glasses. *Metall. Mater. Trans. A* **39**, 1908–1916 (2008).
28. Bondi, K. S. et al. Effects of microalloying with 3d transition metals on glass formation in AlFe alloys. *J. Non-Cryst. Solids* **353**, 4723–4731 (2007).
29. Hoyer, W. & Jödicke, R. Short-range and medium-range order in liquid Au-Ge alloys. *J. Non-Cryst. Solids* **192–193**, 102–105 (1995).
30. Wang, L., Wang, Y. Q., Peng, C. & Zhang, Y. Medium-range structural order in liquid Ni<sub>20</sub>Al<sub>80</sub> alloy: experimental and molecular dynamics studies. *Phys. Lett. A* **350**, 405–409 (2006).
31. Bai, Y. W. et al. Heredity of medium-range order structure from melts to amorphous solids. *J. Appl. Phys.* **112**, 083524 (2012).
32. Khan, S. A., Wang, X. D., Cao, Q. P., Zhang, D. X. & Jiang, J. Z. Structural signature in Au-based amorphous alloys. *Acta Mater.* **140**, 31–38 (2017).
33. Mauro, N. A. et al. Short- and medium-range order in Zr<sub>80</sub>Pt<sub>20</sub> liquids. *Phys. Rev. B* **83**, 1–8 (2011).
34. Mauro, N. A. & Kelton, K. F. Medium range order in Zr-noble metal eutectic liquids. *J. Non-Cryst. Solids* **358**, 3057–3059 (2012).
35. Sheng, H. W., Luo, W. K., Alamgir, F. M., Bai, J. M. & Ma, E. Atomic packing and short-to-medium-range order in metallic glasses. *Nature* **439**, 419–425 (2006).
36. Sheng, H. W. et al. Polyamorphism in a metallic glass. *Nat. Mater.* **6**, 192–197 (2007).
37. Kelton, K. F. et al. First x-ray scattering studies on electrostatically levitated metallic liquids: demonstrated influence of local icosahedral order on the nucleation barrier. *Phys. Rev. Lett.* **90**, 195504 (2003).
38. Sachdev, S. & Nelson, D. R. Theory of the structure factor of metallic glasses. *Phys. Rev. Lett.* **53**, 1947–1950 (1984).
39. Guan, P. F., Fujita, T., Hirata, A., Liu, Y. H. & Chen, M. W. Structural origins of the excellent glass forming ability of Pd<sub>40</sub>Ni<sub>40</sub>P<sub>20</sub>. *Phys. Rev. Lett.* **108**, 1–5 (2012).
40. Park, C., Saito, M., Waseda, Y., Nishiyama, N. & Inoue, A. Structural study of Pd-based amorphous alloys with wide supercooled liquid region by anomalous X-ray scattering. *Mater. Trans. JIM* **40**, 491–497 (1999).
41. Miracle, D. B. The efficient cluster packing model—an atomic structural model for metallic glasses. *Acta Mater.* **54**, 4317–4336 (2006).
42. Holland-Moritz, D. et al. Short-range order in undercooled metallic liquids. *Mater. Sci. Eng. A* **375–377**, 98–103 (2004).
43. Schenk, T., Holland-Moritz, D., Simonet, V., Bellissent, R. & Herlach, D. M. Icosahedral short-range order in deeply undercooled metallic melts. *Phys. Rev. Lett.* **89**, 1–4 (2002).
44. Cheng, Y. Q., Ma, E. & Sheng, H. W. Alloying strongly influences the structure, dynamics, and glass forming ability of metallic supercooled liquids. *Appl. Phys. Lett.* **93**, 111913 (2008).
45. Cheng, Y. Q., Sheng, H. W. & Ma, E. Relationship between structure, dynamics, and mechanical properties in metallic glass-forming alloys. *Phys. Rev. B* **78**, 1–7 (2008).
46. Egami, T. & Billinge, S. J. L. *Underneath the Bragg Peaks Structural Analysis of Complex Materials*. Volume 16 (Pergamon, 2012).
47. Liu, X. J. et al. Metallic liquids and glasses: atomic order and global packing. *Phys. Rev. Lett.* **105**, 1–4 (2010).
48. Fang, X. W. et al. Spatially resolved distribution function and the medium-range order in metallic liquid and glass. *Sci. Rep.* **1**, 19–21 (2011).
49. Ding, J., Ma, E., Asta, M. & Ritchie, R. O. Second-nearest-neighbor correlations from connection of atomic packing motifs in metallic glasses and liquids. *Sci. Rep.* **5**, 1–9 (2015). <https://doi.org/10.1038/srep17429>.
50. Pan, S. P., Qin, J. Y., Wang, W. M. & Gu, T. K. Origin of splitting of the second peak in the pair-distribution function for metallic glasses. *Phys. Rev. B* **84**, 092201 (2011).
51. Bennett, C. H. Serially deposited amorphous aggregates of hard spheres. *J. Appl. Phys.* **43**, 2727–2734 (1972).
52. Gaskell, P. H. A new structural model for transition metal-metalloid glasses. *Nature* **276**, 484–485 (1978).
53. Schroers, J. & Johnson, W. L. Ductile bulk metallic glass. *Phys. Rev. Lett.* **93**, 255506 (2004).
54. Lewandowski, J. J., Wang, W. H. & Greer, A. L. Intrinsic plasticity or brittleness of metallic glasses. *Philos. Mag. Lett.* **85**, 77–87 (2005).
55. Kuball, A. et al. On the bulk glass formation in the ternary Pd-Ni-S system. *Acta Mater.* **158**, 13–22 (2018).
56. Kuball, A., Gross, O., Bochtler, B. & Busch, R. Sulfur-bearing metallic glasses: a new family of bulk glass-forming alloys. *Scr. Mater.* **146**, 73–76 (2018).
57. Dippel, A. C. et al. Beamline P02.1 at PETRA III for high-resolution and high-energy powder diffraction. *J. Synchrotron Radiat.* **22**, 675–687 (2015).
58. Hammersley, A. P. FIT2D: an introduction and overview. *ESRF Intern. Rep.* ESRF97HA02T 1–33 (1997).
59. Qiu, X., Thompson, J. W. & Billinge, S. J. L. PDFgetX2: a GUI-driven program to obtain the pair distribution function from X-ray powder diffraction data. *J. Appl. Crystallogr.* **37**, 678 (2004).
60. Faber, T. E. & Ziman, J. M. A theory of the electrical properties of liquid metals. *Philos. Mag.* **11**, 153–173 (1964).
61. Wei, S. et al. Structural evolution on medium-range-order during the fragile-strong transition in Ge<sub>15</sub>Te<sub>85</sub>. *Acta Mater.* **129**, 259–267 (2017).

### Acknowledgements

We acknowledge DESY (Hamburg, Germany), a member of the Helmholtz Association HGF, for the provision of experimental facilities. Parts of this research were carried out at PETRA III and we would like to thank Jo-Chi Tseng for the assistance in using the P02.1 beamline and for the temperature calibration. We are grateful to I. Gallino for useful discussions.

### Author contributions

O.G. and R.B. conceived the study. N.N., A.K. and O.G. prepared the samples. O.G., N.N., A.K., B.B., S.H. and M.F. planned and conducted the synchrotron X-ray experiments. O.G. analyzed the data and wrote the paper with input from R.B., N.N., A.K., B.B., S.H. and M.F. All authors contributed extensively to the discussion.

### Additional information

**Supplementary information** accompanies this paper at <https://doi.org/10.1038/s42005-019-0180-2>.

**Competing interests:** The authors declare no competing interests.

**Reprints and permission** information is available online at <http://npg.nature.com/reprintsandpermissions/>

**Publisher's note:** Springer Nature remains neutral with regard to jurisdictional claims in published maps and institutional affiliations.

 **Open Access** This article is licensed under a Creative Commons Attribution 4.0 International License, which permits use, sharing, adaptation, distribution and reproduction in any medium or format, as long as you give appropriate credit to the original author(s) and the source, provide a link to the Creative Commons license, and indicate if changes were made. The images or other third party material in this article are included in the article's Creative Commons license, unless indicated otherwise in a credit line to the material. If material is not included in the article's Creative Commons license and your intended use is not permitted by statutory regulation or exceeds the permitted use, you will need to obtain permission directly from the copyright holder. To view a copy of this license, visit <http://creativecommons.org/licenses/by/4.0/>.

© The Author(s) 2019